Proceedings of the 16th European VLBI Network Symposium
Ros, E., Benke, P., Dzib, S., Rottmann, I., & Zensus, J.A. (eds.)
September 2nd-6th 2024, Bonn, Germany

A multiscale and multi-frequency radio study of local U/LIRGs

G. Lucatelli[1], R. J. Beswick[1], J. Moldón[2], A. Alberdi[2], M. Á. Pérez-Torres[2,3], and S. del Palacio[4]

[1] Jodrell Bank Centre for Astrophysics, The University of Manchester, Manchester M13 9PL, UK
[2] Instituto de Astrofísica de Andalucía (IAA-CSIC), Glorieta de la Astronomía s/n, 18008 Granada, Spain
[3] Facultad de Ciencias, Universidad de Zaragoza, Pedro Cerbuna 12, E-50009 Zaragoza, Spain
[4] Department of Space, Earth and Environment, Chalmers University of Technology, Gothenburg, Sweden

Abstract. We analyse the radio emission, star formation and nuclear activity in local Luminous and Ultra-Luminous Infrared Galaxies (U/LIRGs, $z < 0.1$) using *e*-MERLIN and VLA radio data (1.4–33 GHz). Through multiscale and multi-frequency decomposition, we apply a broadband spectral energy distribution (SED) fitting. We distinguish between extended star-forming regions and compact AGN cores, quantifying non-thermal spectral index, and the thermal and non-thermal emission components, across kiloparsec and parsec scales. This study underscores the potential of multiscale radio SED analysis to probe complex processes in U/LIRGs.

1. Introduction

Understanding the physical processes driving star formation (SF) and nuclear activity in galaxies still remains a challenge. Luminous and Ultra-Luminous Infrared Galaxies (U/LIRGs) represent extreme cases of these phenomena, characterised by their high infrared luminosities ($L_{\rm IR} > 10^{11}\,L_{\odot}$), typically resulting from intense SF activity and/or active galactic nuclei (AGN) (Condon 1992; Sanders & Mirabel 1996; Pérez-Torres 2021). Local U/LIRGs ($z < 0.1$) serve as crucial laboratories for understanding these processes, as their proximity allows for detailed spatial resolution of their structure across multiple wavelengths using interferometric observations. These systems can represent the final stages of major galaxy mergers, where gravitational interactions transport gas toward the central regions, triggering both starburst activity and AGN feedback (Farrah 2003). Yet, $\sim$20% of local U/LIRGs are isolated spiral galaxies (Haan 2011), and what induces intense activity is yet to be understood. However, disentangling the relative contributions of SF and AGN activity remains challenging, particularly in the heavily dust-obscured nuclear regions (Linden et al. 2019). Radio observations provide a dust-unbiased tool to study U/LIRGs by penetrating the dense material obscuring their central regions. Combining interferometers like *e*-MERLIN and the VLA enables decomposition of the radio emission across scales—from extended star-forming regions to nuclear starbursts and compact AGN cores—allowing systematic study of galaxy-wide processes at kpc–scales down to nuclear activity at pc–scales. At each scale, the radio spectrum reveals distinct components: thermal free-free emission from ionised gas (e.g. H_{II} regions), non-thermal synchrotron emission from diffuse cosmic-rays (predominantly accelerated in supernova remnants) and AGN related emission. In this work, we present a comprehensive analysis of local U/LIRGs using a multiscale approach to decompose their radio emission. Our primary goal is to establish resolved and accurate SF rates (SFR) while accounting for any AGN contribution. The methods and science presented in this work can be used with any other combination of instruments, aiming to probe the multiscale structure of galaxies.

2. *e*-MERLIN and VLA Observations

The *e*-MERLIN observations were conducted as part of the *e*-MERLIN Legacy Project between 2015 and 2020, at frequencies of 1.4 and 6.0 GHz. With angular resolutions of ~ 0.2" and ~ 0.05", respectively, these observations are essential for probing the nuclear regions of U/LIRGs at low frequencies. To characterise the same spatial scales at higher frequencies, we use VLA observations at 15, 22 and 33 GHz in the A-configuration. With this set of data, we can continuously map the emission on nuclear regions ($\lesssim$ 300 pc), from 1.4 up to $\sim$33 GHz. On larger angular scales $\gtrsim 0.3$", observations from mixed VLA configurations are used to track the emission in the full frequency range of 1–33 GHz. We use 1–12 GHz observations taken with the A configuration, and 15–33 GHz observations taken with the C configuration. Data calibration was made with the *e*-MERLIN CASA Pipeline[1] (CASA v.5.7) and with the EVLA CASA pipeline[2] (v.6.5). Continuum imaging was made with WSClean (v3.4) (Offringa et al. 2014).

3. Results and Discussion

3.1. Morphological Analysis and Image Decomposition

The morphological characteristics of radio emission regions vary significantly with both frequency and spatial scale. We implement a systematic approach to quantify

[1] `https://github.com/e-merlin/eMERLIN_CASA_pipeline`
[2] `https://science.nrao.edu/facilities/vla/data-processing/pipeline`

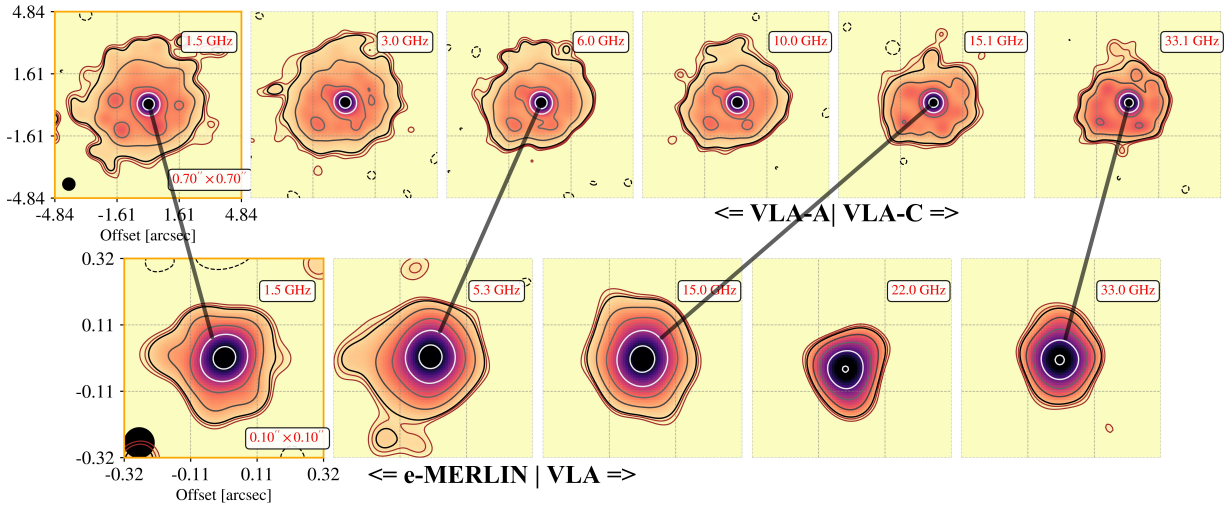

Fig. 1. Multiscale and multi-frequency beam-*uv*-matched images of Mrk 331. The top row shows the larger scales of the emission (unresolved core and the extended emission). The lower row shows maps with *e*-MERLIN (1-6 GHz) and VLA ($15-33$ GHz), highlighting the nuclear region (C1). Offsets are relative to *e*-MERLIN pointing RA=23:51:26.74, DEC=+20.35.10.30.

these variations, extracting relevant information from each structure, and also decompose complex regions via component image fitting. This is done for any spatial scale and frequency, thus we capture individual properties along these two axes. The code used for this analysis and image decomposition is MORPHEN[3] (Lucatelli et al. 2024).

3.2. Broadband Radio SED analysis

Analysing radio emission in U/LIRGs requires a multiscale approach to capture each physical mechanism involved. Our method combines spectral and spatial information across frequencies and scales, enabling decomposition of the emission into its components. A spectrum consisting of synchrotron and free-free emission is given by $S_\nu = A_{\rm sy}(\nu/\nu_0)^{\alpha_{\rm sy}} + A_{\rm ff}(\nu/\nu_0)^{-0.1}$, where $\nu_0 = 10$ GHz is the reference frequency, $A_{\rm sy}$ and $A_{\rm ff}$ are scaling factors for the synchrotron and free-free components, and $\alpha_{\rm sy}$ is the synchrotron spectral index. We adopt the canonical spectral index of $\alpha_{\rm ff} = -0.1$ for optically thin free-free emission. The emitted SED can be significantly affected at low frequencies due to FF absorption (FFA) in the ionised gas. For simplicity, we assume a diffuse, homogeneous absorbing medium. The effects of a clumpy medium can be relatively similar but include additional free parameters and are not likely to be constrained without observations at $\nu \lesssim 1.0$ GHz (Lacki 2013; Ramírez-Olivencia et al., 2022). Assuming a homogeneous medium, the absorbed synchrotron spectrum is attenuated by $S^{\rm sy}_\nu = A_{\rm sy}(\nu/\nu_0)^{\alpha_{\rm sy}} e^{-\tau_\nu}$ where $\tau_\nu = (\nu/\nu_{\rm t})^{-2.1}$ is the optical depth at frequency ν with a turnover frequency $\nu_{\rm t}$. The homogeneous free-free absorbed spectrum follows $S^{\rm ff}_\nu = A_{\rm ff}(\nu/\nu_0)^{-0.1}(1-e^{-\tau_\nu})/\tau_\nu$.

[3] Development version available at `https://github.com/lucatelli/morphen/tree/dev`.

The analysis of the radio SED at different spatial scales provides crucial insights about the physical processes associated. We identify compact, flat-spectrum cores indicative of AGN activity at scales $\lesssim 10$ pc. We can also map the extended synchrotron emission at scales $\gtrsim 500$ pc and characterize the thermal fraction in star-forming regions at individual regions of size ~ 100–200 pc. In Figure 1 we provide beam- and *uv*-matched images of Mrk 331, at two representative spatial scales. Linked to these images, we show the SED results in Figure 2. The nuclear region (C1) of Mrk 331 shows a steep $\alpha_{\rm sy}$, indicative of a starburst region. The extended emission has a well defined $\alpha_{\rm sy}$, typical of synchrotron-dominated SF regions. The minimisation of parameters $(A_{\rm ff}, A_{\rm sy}, \alpha_{\rm sy})$ for the SED decomposition is done via Markov Chain Monte Carlo (MCMC) simulations. The implementation is contained within the code RADIOSED-FITTER[4].

3.3. Thermal Fractions and Star formation rates

From the broadband SED analysis, we extract physical information regarding the most recent star formation activity happening in our sources. The spectrum shown in Figure 2 (right panel) for Mrk 331, shows that at ~ 33 GHz, thermal emission is dominant. From the posterior distributions of the flux densities from the MCMC results shown in Figure 3, we can derive the thermal fraction at a given frequency via $f_{\rm th}(\nu) = A_{\rm ff}(\nu/\nu_0)^{-0.1}/S_\nu$. We accurately infer a global thermal fraction of $f^{33}_{\rm th} = 0.52^{+0.13}_{-0.14}$.

Using the calibrations from radio fluxes to SFR from Murphy et al. (2011), we can determine the rate at which stars form, probed by synchrotron and free-free emission.

[4] The code was originally developed for del Palacio et al. (2024) and will be made public upon acceptance of an ongoing work.

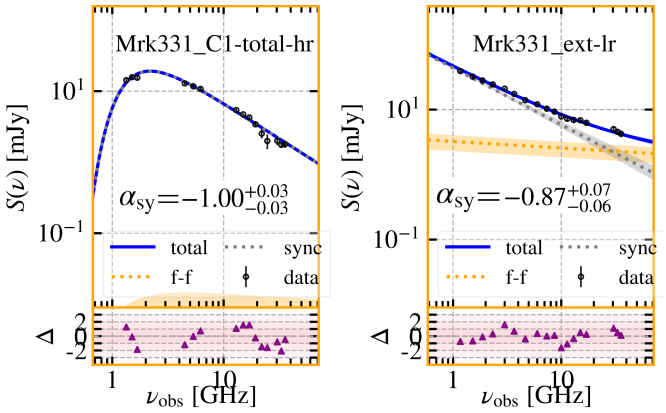

Fig. 2. SED decomposition of the nuclear region (C1) on the left (high-resolution), and the extended emission of Mrk 331 on the right (low-resolution). The extended emission is obtained by removing the core region via image decomposition. The steep spectrum of the core is an indicative of a dense starburst region.

The thermal emission probes the most recent SF activity (Kennicutt & Evans 2012), on a timescale of 1–10 Myr, and can contribute significantly to the total radio fluxes on frequencies above ~ 20 GHz. The SFR on the timescale of 30–100 Myr is given by the synchrotron component (Bressan et al. 2002). From the posterior distributions of the SED for the fluxes (see Figure 4) we obtain $\mathrm{SFR_{ff}} = 11.7^{+2.8}_{-3.4}$ $\mathrm{M_\odot\ yr^{-1}}$ and $\mathrm{SFR_{sy}} = 22.9^{+5.4}_{-4.0}$ $\mathrm{M_\odot\ yr^{-1}}$.

3.4. Maps for Spectral Index and Thermal Fractions

In order to obtain more accurate information about the morphology of a source, we can use the broadband spectrum on a pixel-by-pixel basis. Computing the SED in each pixel reveals the distribution of regions with high and low thermal fractions, allowing also to understand how the non-thermal spectral index (α_{sy}) varies along the source. In Figure 5 we present the spectral index map for NGC 7674, on higher resolution angular scales. The region with flatter α reveals the existence of an AGN core. The two jet regions (lobes and hot-spots) have steeper α, ~ -1.0. In Figure 6, we have determined the thermal fraction map of Mrk 331, fitting pixel-by-pixel SY+FF spectrum model to all images. The intensity profiles for the non-thermal spectral index and thermal fraction are displayed in Figure 7.

4. Conclusions and Future Work

We have presented a complete synthesis for the analysis of local U/LIRGs, with Mrk 331 as the prototype. With this set of techniques and data, we were able to decompose the radio emission in individual structures, and also separate emission mechanisms with broadband spectral energy decomposition. Accurate measures for thermal fraction and SFR were obtained. Lucatelli et al. (in prep.) will present the same analysis discussed here, but for multiple local

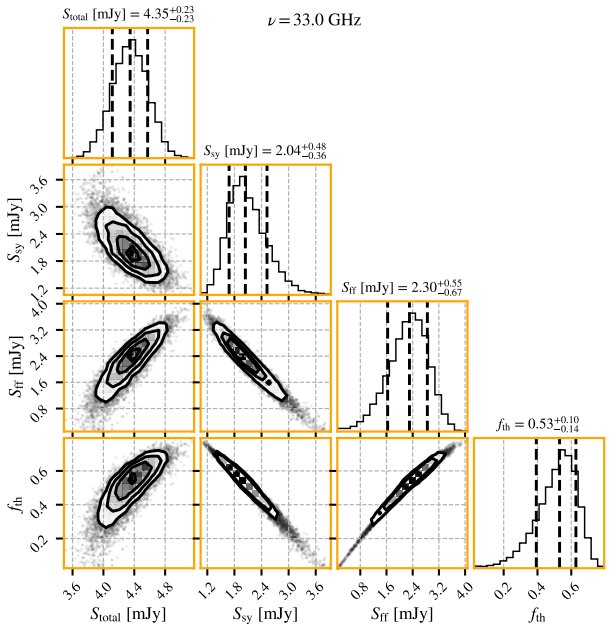

Fig. 3. Posterior distributions for each component of the fluxes (synchrotron and free-free), obtained via the MCMC sampling.

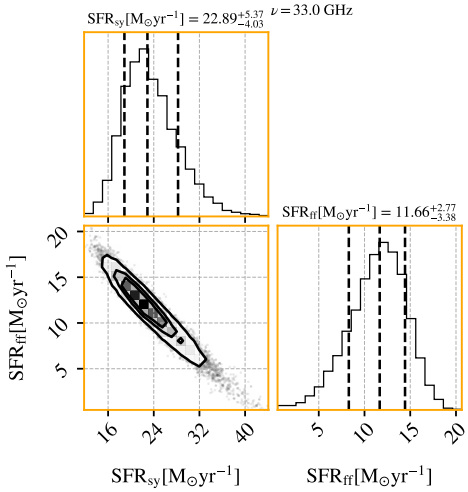

Fig. 4. Global extended large-scale decomposed SFR from synchrotron and free-free emission for Mrk 331.

U/LIRGs. The next step will be to amend VLBI/EVN to this study, so that we can map a wider set of spatial scales, and thus having more constraints about the nature of the radio emission on pc scales.

Acknowledgements. The European VLBI Network (www.evlbi.org) is a joint facility of independent European, African, Asian, and North American radio astronomy institutes. We would like to acknowledge the support of the *e*-MERLIN Legacy project "LIRGI", upon which this study is based. We acknowledge financial support from Grant LINKB20064 (Spanish National Research Council Program of Scientific Cooperation for Development i-LINK+2020). Author G. Lucatelli acknowledges financial support for a PhD studentship from STFC; and the Spanish Prototype of an SRC (SPSRC) service and support funded by the

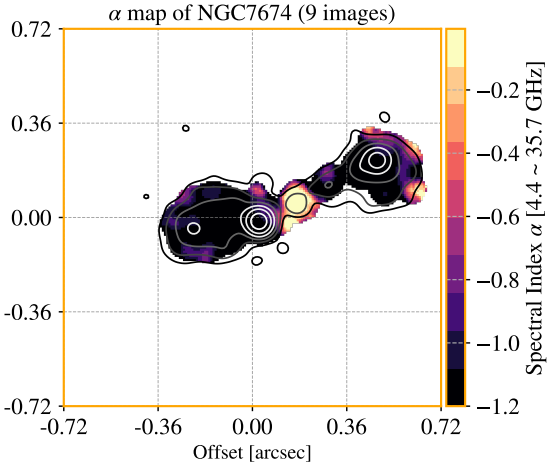

Fig. 5. Spectral index map for the Seyfert II galaxy NGC 7674, highlighting the AGN core with a flat spectral index of $\alpha \sim -0.1$. The contours refer to the *e*-MERLIN map at 6 GHz.

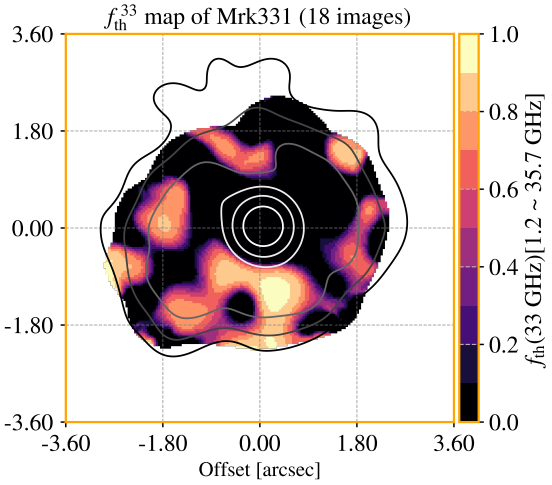

Fig. 6. Thermal fraction map at 33 GHz for Mrk 331, revealing that the south region contains higher thermal fractions.

Ministerio de Ciencia, Innovación y Universidades (MICIU), by the Junta de Andalucía, by the European Regional Development Funds (ERDF) and by the European Union NextGenerationEU/PRTR. The SPSRC acknowledges financial support from the Agencia Estatal de Investigación (AEI) through the "Center of Excellence Severo Ochoa" award to the Instituto de Astrofísica de Andalucía (IAA-CSIC) (SEV-2017-0709) and from the grant CEX2021-001131-S funded by MICIU/AEI/ 10.13039/501100011033. *e*-MERLIN is a National Facility operated by the University of Manchester at Jodrell Bank Observatory on behalf of STFC. The National Radio Astronomy Observatory is a facility of the National Science Foundation operated under cooperative agreement by Associated Universities, Inc. SdP acknowledges support from ERC Advanced Grant 789410.

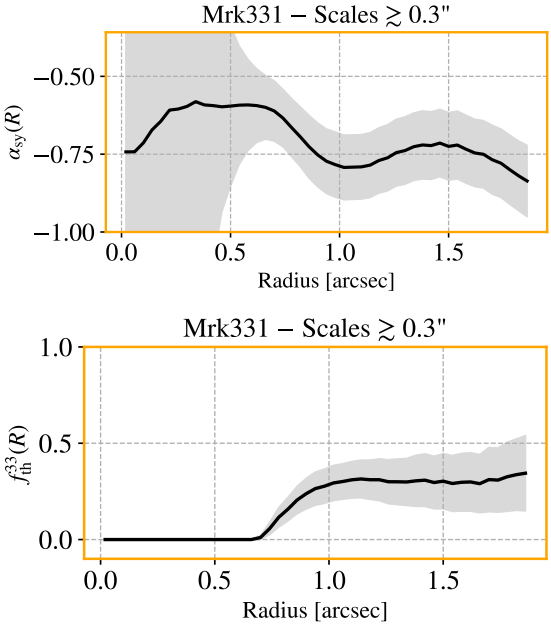

Fig. 7. The variation of the non-thermal spectral index (top) and the thermal fraction (bottom) at 33 GHz, as a function of projected radius, for Mrk 331.

References

Bressan, A., Silva, L., Granato, G. L. 2002, A&A, 392, 377
Condon, J. J. 1992, ARA&A, 30, 575–611
del Palacio, S., Aalto, S., Yang, C., et al. 2024, in EAS Conf. Ser., EAS2024, 1310
Farrah, D., Afonso, J., Efstathiou, A., et al., 2003, MNRAS, 343, 585–607
Haan, S., Surace, J. A., Armus, et al. 2011, AJ, 141, 100
Kennicutt, R. C., Evans, N. J. 2012, ARA&A, 50, 531–608
Lacki, B. C. 2013, MNRAS, 431, 3003–3024
Lucatelli, G., Beswick, R. J., Moldón, J., et al. 2024, MNRAS, 529, 4468
Linden, S. T., Song, Y., Evans, A. S., et al. 2019, ApJ, 881, 70
Murphy, E. J., Condon, J. J., Schinnerer, E., et al. 2011, ApJ, 737, 67
Offringa, A. R., McKinley, B., Hurley-Walker, N., et al. 2014, MNRAS, 444, 606–619
Pérez-Torres, M. A., Mattila, S., Alonso-Herrero, A., Aalto, S., Efstathiou, A. 2021, AApR, 29, 1
Ramírez-Olivencia, N., Varenius, E., Pérez-Torres, M. A., et al. 2022, A&A, 658, A4
Sanders, D. B., Mirabel, I. F. 1996, ARA&A, 34, 749